

DESIGN OF A MACH-15 TOTAL-ENTHALPY NOZZLE WITH NON-UNIFORM INFLOW USING ROTATIONAL MOC

Richard L. Gaffney, Jr. *

NASA Langley Research Center, Hampton, Virginia, 23681-2199, U.S.A

A new computer program to design nozzles with non-uniform inflow has been developed using the rotational method of characteristics (MOC). This program has been used to design a nozzle for the NASA's HYPULSE shock-expansion tunnel for use in scramjet engine tests at a Mach-15 flight-enthalpy condition. The nozzle has an area ratio of 9.5:1 that expands the inflow from Mach 6 along the centerline to Mach 8.7. Although the density and Mach number vary radially at the exit due to the non-uniformities of the inflow, the MOC procedure produces exit flow that is parallel and has uniform static pressure. The design has been verified with CFD which compares favorably with the MOC solution.

I. Introduction

With the NASA's successful development and flight test of scramjet engine designs at Mach 7 and 10, attention has turned to the design and testing of a Mach-15 scramjet engine. Much of the Mach-10 scramjet engine testing was done in the NASA's HYPULSE shock-expansion tube facility located at ATK-GASL in Ronkonkoma, New York. As the Mach 10 tests were coming to a conclusion, several runs were made at a Mach-15 flight-enthalpy condition in order to evaluate test possibilities for a Mach-15 scramjet engine design. The facility nozzle used in the Mach 10 tests was replaced by a conical flow nozzle that was designed for a Mach-21 flight-enthalpy aerothermodynamic test. This nozzle produced a test flow with properties that varied both radially and axially, which was undesirable for engine testing. Since the heat loads in a pulse facility are low, nozzles can be made of fiberglass and are relatively inexpensive to manufacture. With this in mind, a decision was made to design and build a new nozzle for future Mach-15 flight-enthalpy-condition tests.

The design of a nozzle for the HYPULSE facility operating in expansion tunnel mode is challenging because the flow at the exit of the expansion tube is non-uniform due to viscous effects. Several options were considered for the method (and code) to be used to develop the new design. Korte¹ has developed a way of using Sivells' irrotational method of characteristics (MOC) code² for high-temperature flows in which there is significant variation in the ratio of specific heats in the nozzle. However, using Sivells' program would require significant modification to the FORTRAN 66 code to allow for non-uniform inflow and a rotational flowfield.

A second option was to use Korte's CAN-DO code³ that fits the nozzle contour with a spline and adjusts the spline points to give optimal exit flow. In this code, the flowfield is analyzed with a parabolized Navier-Stokes solver. This method has the advantage that viscous effects are included in the optimization process.

* Aerospace Engineer, Hypersonic Air breathing Propulsion Branch, Senior Member AIAA.

Copyright © 2005 by the American Institute of Aeronautics and Astronautics, Inc. The U.S. Government has a royalty-free license to exercise all rights under the copyright claimed herein for Governmental purposes. All other rights are reserved by the copyright owner.

It has the disadvantage of being limited by the number of control points used in the optimization process and it requires much more computer time than an MOC solver. In addition, the code must be modified for each specific case being considered.

A third option was to write a new computer program to solve the Euler equations using the rotational MOC. This option has the advantage of not being limited by the structure (or programming language) of an existing code, not having to work through a program line by line in order to make the necessary modifications, it is relatively fast to run and the number of points defining the contour depends on the number of initial points (user specified). Although this option does not directly take into account viscous effects, the non-uniform profiles of the total properties entering the HYPULSE nozzle are created by viscous effects and are maintained by solving the rotational equations. Final viscous corrected contours can be generated by iterating the MOC solution with a full Navier-Stokes solution⁴ (usually only one or two iterations). This paper will present the details of the rotational method of characteristics applied to general nozzle design followed by a discussion of how the computer program was applied specifically to the design of a nozzle for the HYPULSE facility.

II. Rotational MOC

Facility nozzles for aerodynamic tests are usually designed to process flow at near stagnation conditions and produce uniform exit flow at the design Mach number. In these circumstances, all of the flow properties at the inflow of the nozzle are uniform. For hypervelocity tests, stagnating the flow is not a practical solution as the total temperature is high enough to cause the flow to dissociate and the pressure is difficult to contain. Shock-expansion facilities, such as HYPULSE,⁵ are able to generate high-speed, high-enthalpy flow without stagnating the flow. However, the HYPULSE expansion tube is only six inches in diameter and viscous effects reduce the size of the usable core flow to about three inches or less. By processing the tube-exit flow through a nozzle, the size of the core flow can be increased allowing for larger test articles. Unfortunately, the viscous effects not only reduce the size of the core flow, they also cause the flow to be heavily profiled (non-uniform). This significantly complicates the design of the nozzle. Fortunately the method of characteristics, which has been used extensively in nozzle design, can also be used in this case.

In a supersonic isentropic nozzle flow with constant total properties, the flow is irrotational. The governing fluid equation is the compressible potential equation which can be solved using the method of characteristics. For axisymmetric flows, this involves solving two ordinary differential equations (compatibility equations) along left and right running characteristic curves (one equation along each characteristic). Equations for the two characteristics curves are solved with the two compatibility equations.

If the total conditions are non-uniform at inflow, the flow is rotational and the Euler equations must be solved. Fortunately, for supersonic isentropic flow they can also be solved using the MOC. However, there are four ordinary differential equations that must be solved along three characteristic curves. Following the work of Zucrow and Hoffman,⁶ the compatibility equations for the rotational MOC are

$$\rho V \, dV + dP = 0 \quad (1)$$

$$dP - a^2 \, d\rho = 0 \quad (2)$$

and

$$\frac{(\sqrt{M^2 - 1}) \, dP}{\rho V^2} \pm d\theta + \delta \left[\frac{\sin \theta \, dx}{r \, M \cos(\theta \pm \mu)} \right] = 0 \quad (3)$$

where ρ is the density, V is the magnitude of the velocity, P is the pressure, a is the speed of sound, M is the Mach number, θ is the flow angle, μ is the Mach angle, x is the axial coordinate and r is the radial distance from the centerline. The term δ in equation 3 is zero for two-dimensional flow and one for axisymmetric

flow. Compatibility equations 1 and 2 hold along the streamline whose characteristic equation is

$$\frac{dr}{dx} = \tan \theta \quad (4)$$

while compatibility equation 3 holds along left and right running Mach lines given by

$$\frac{dr}{dx} = \tan (\theta \pm \mu) \quad (5)$$

For calorically perfect gas flows the compatibility equations can be recast in a different form with some manipulation:

$$dP_o = 0 \quad (6)$$

$$d\rho_o = 0 \quad (7)$$

and

$$d(\nu \pm \theta) - \frac{dP_o}{\gamma P_o M^2 \tan \mu} - \delta \left[\frac{\sin \mu \sin \theta dr}{r \sin (\theta \mp \mu)} \right] = 0 \quad (8)$$

where P_o and ρ_o are the total pressure and total density, γ is the ratio of specific heats and ν is the Prandtl-Meyer function.⁷ This form of the equations is similar to that used by Genkin, Baer and Falcovitz⁸ and has the advantage of no discretization error for the streamline compatibility equations.

Equations 6 and 7 are the compatibility equations that hold along a streamline (equation 4). These equations can be solved exactly with the result that the total conditions are constant along a streamline. Equation 8 is the compatibility equation that holds along the left and right running Mach lines (equation 5). The second term in the equation is due to the rotationality of the flow. If the total pressure is constant in the flow, this term is zero. The third term in the equation is the axisymmetric source term. For the special case of two-dimensional, irrotational flow the second and third terms are zero and the equation can be solved exactly.

These equations are solved numerically by discretization of the equations on a grid created by intersecting characteristic lines, such as that shown in figure 1. The discretization of the equations is that given by Anderson⁷ and involves two adjacent points in the grid. (Each equation involves its own pair of grid points.) Differentials in the equation are replaced with first order backward differences and all other terms are averages between the two points. For example, the second term in equation 8 is discretized as

$$\frac{P_{o2} - P_{o1}}{\gamma \overline{P_o} \overline{M}^2 \tan \overline{\mu}} \quad (9)$$

where the over-bar denotes the arithmetic average:

$$\overline{\phi} = \frac{\phi_1 + \phi_2}{2} \quad (10)$$

Each equation is discretized along the appropriate characteristic curve and involves one known point and one unknown point, which results in a system of coupled non-linear algebraic equations that are solved simultaneously using a Newton-Raphson method. Because the flow is supersonic, solution points can be computed sequentially. For nozzle design, the solution at points that depend on the inflow and the user-specified expansion portion of the nozzle (the blue region in figure 1, also called the kernel) are computed first. The turning contour and the points dependent on it (the green region in figure 1) are then computed. The solution procedure at each point depends on the type of point being solved, interior, centerline, surface point, etc.. The unit processes for interior, centerline and known surface points are detailed in the textbook by Zucrow and Hoffman.⁶ The unit processes for determining the turning contour were developed by the author. For completeness, each of the unit processes is discussed below.

A. Interior point

The solution geometry of an interior point in the kernel is illustrated in figure 2. The location and properties of points 1 and 2 are known. Point 4, which is the new point, is located at the intersection of the C^+ characteristic running through point 1 and the C^- characteristic running through point 2. Point 3 lies at the intersection of the line connecting points 1 and 2 and the streamline passing through point 4. The properties at point 3 are linearly interpolated from points 1 and 2. Given this geometry, equations 1-3 are discretized using the appropriate points. The resulting equation set is then solved, yielding the location and properties of point 4 (and point 3 in the process).

B. Centerline point

The solution geometry of a point on the centerline is illustrated in figure 3. The location and properties of points 1 and 2 are known. Point 3, which is the new point, is located at the intersection of the C^- characteristic running through point 2 and the centerline ($r = 0$), which is also a streamline. The compatibility equation along the C^+ characteristic is replaced by the boundary condition $\theta_3 = 0$. Since the centerline is also a streamline, the total properties at point 3 equal the total properties at point 1 leaving only one unknown property (M) which is determined by solving the compatibility equation along the C^- characteristic.

C. Nozzle Surface

The solution geometry of a point on the nozzle surface in the user-specified expansion region is illustrated in figure 4. The location and properties of points 1 and 2 are known. Point 3, which is the new point, is located at the intersection of the C^+ characteristic running through point 1 and the known nozzle surface which is also a streamline. For this type of solution geometry the C^- compatibility equation is replaced by the boundary condition

$$\theta_3 = \left. \frac{dr}{dx} \right|_{\text{nozzle surface}} \quad (11)$$

Since point 3 lies on the same streamline as point 2, the total properties at point 3 equal the total properties at point 2. The remaining properties at point 3 are determined by simultaneously solving the compatibility equation along the C^+ characteristic and determining the intersection of the C^+ characteristic with the given nozzle surface, $r = f(x)$.

D. Final C^+ Characteristic

Once points in the kernel have been computed, points in the turning region can be computed. This is accomplished by first computing the solution at a point on the final (terminating) C^+ characteristic. The point arrangement of this solution step is illustrated in figure 5. The solutions at points 1, 2 and 3 are known. Point 5 is the new unknown point. It is located at a user-specified distance from point 1 along the final characteristic. Point 4 is located at the intersection of the line between points 2 and 3 and the streamline running through point 5. The properties at point 4 are linearly interpolated from points 2 and 3. Since there is no C^- characteristic, the user is free to specify one flow property. The solution of the resulting equation set yields the properties at point 5 (and point 4).

Ideally, one would like the nozzle exit flow to be parallel and be as uniform as possible. If the user specifies that $\theta = 0$ along the final characteristic, equation 3 gives $dP = 0$ and the flow at the nozzle exit is both parallel and has uniform static pressure.

E. Interior Point - Turning Contour

Once the solution of a point on the final characteristic has been computed, points in the interior are computed sequentially, moving from the final characteristic upstream along a C^- characteristic to the nozzle surface.

The geometry for this situation is shown in figure 6. The solutions at points 1, 2, 3 and 4 are known while the solution at point 6 is unknown. Point 6 is located at the intersection of the C^- characteristic running through point 1 and the C^+ characteristic running through point 2. Point 5 is located at the intersection of the line connecting points 3 and 4 and the streamline running through point 6. The properties at point 5 are linearly interpolated from points 3 and 4. The solution of the discretized equations yields the properties at point 6 (and point 5).

F. Surface Point - Turning Contour

As stated previously, the solution of interior points in the turning region starts at the final characteristic and progresses upstream along the C^- characteristic. Near the nozzle surface, a place is reached where the new point, located at the intersection of the C^+ and C^- characteristics, lies outside of the flowfield. This situation is recognized when the computer program cannot find any points on a streamline upstream of the new point. When this happens, the new point must be a surface point, which is shown graphically in figure 7. In this case, points 1 and 2 are known and point 3 is the new unknown surface point. The surface point is positioned along the C^- characteristic which runs through point 1 at a location where the mass flow computed (using the trapezoidal rule) along the C^- characteristic matches the mass flow at inflow. The line connecting points 2 and 3 is the surface, which is also a streamline. The solution of the discretized equations and the mass flow requirement yields the properties and location of point 3.

After a surface point is computed, the solution procedure returns to the final characteristic and computes a new row of points along the next C^- characteristic. This procedure is repeated until the surface and the final characteristic intersect.

G. Numerical Considerations

There are several sources of error that are introduced as part of the numerical process. This includes both discretization errors and convergence errors. The discretization errors are fixed by the desire to limit the number of points associated with each calculation, which greatly reduces the complexity of solving equations 4-8. Convergence errors are limited by applying the iterative procedure at each unknown point until the absolute value of the maximum residual of equations 6-8 is less than 1.0×10^{-10} .

Since the numerical scheme is sequential in nature, errors can build up as the solution progresses downstream. At the higher Mach numbers, where the characteristic lines are long and very shallow, these errors can produce small perturbations in the contour near the end of the nozzle (where the Mach number is highest). In high-Mach-number flows these irregularities, which may be too small to detect with the human eye, can produce pressure waves and non-uniform flow at the nozzle exit. In order to avoid this, the first and second derivatives of the nozzle contour are examined as a post processing step. If perturbations are identified, the contour near the exit is smoothed using a Savitzky-Golay smoothing filter.⁹

One other problem that can occur in an MOC solution is that of characteristic lines of the same family converging. This situation occurs when a shock-wave forms in the flowfield (which violates the MOC isentropic flow assumption). The convergence can also be the result of numerical errors. If characteristic lines are close together, small errors can cause them to converge or even cross. This problem tends to occur when the user, in an attempt to reduce discretization errors, uses a large number of characteristics in the calculation. Whether real or numerical, dealing with converging or crossing characteristic lines increases the complexity of the solution procedure. The current program handles crossed C^+ characteristic lines near the nozzle exit by dropping one of the lines from the characteristic net. If more than two lines converge or cross, the program stops.

H. MOC Verification

A verification of the MOC code was done by designing a nozzle with a non-uniform inflow. The inflow conditions were a constant static pressure and static density of 200 kPa and 0.5 kg/m^3 respectively and a

Mach number which varied linearly from 2.0 at the centerline to 1.01 at the wall. These conditions result in non-linear profiles of total pressure and total density as shown in figure 8. The target nozzle was designed to have a centerline exit Mach number of 5.0, a constant exit static pressure and parallel exit flow. For this case the gas constant was set to 287.06 and γ was set to 1.4. The initial expansion surface (from the throat to the inflection point) was specified as a Gaussian curve with a radius of curvature at the throat of 5.0. For these conditions, the exit profiles can be determined analytically. By design, the exit flow angle is zero and the static pressure is constant. From the isentropic nature of the flowfield, the exit total pressure and total density profiles are similar to those at the nozzle inflow, having the same values (along a streamline) but different radial distributions. The relationship between the radius of an inflow streamline (R_{inflow}) and the radius of the same streamline at the nozzle exit (R_{exit}) is

$$R_{\text{exit}}^2 = 2 \sqrt{\frac{P_{\text{inflow}}}{P_{\text{exit}}}} \int_0^{R_{\text{inflow}}} \left[\sqrt{\frac{\rho_{\text{inflow}}}{\rho_{\text{exit}}}} \left(\frac{M_{\text{inflow}}}{M_{\text{exit}}} \right) r \right] dr \quad (12)$$

where M_{inflow} is a known distribution. By equating the exit total pressure to the inflow total pressure (along a streamline) the following relationship between the inflow and exit Mach numbers can be derived:

$$M_{\text{exit}} = \sqrt{\frac{2}{\gamma - 1} \left\{ \left(\frac{P_{\text{inflow}}}{P_{\text{exit}}} \right)^{\frac{\gamma-1}{\gamma}} \left[1 + \left(\frac{\gamma-1}{2} \right) M_{\text{inflow}}^2 \right] - 1 \right\}} \quad (13)$$

For a constant inflow density, the density ratio is

$$\frac{\rho_{\text{inflow}}}{\rho_{\text{exit}}} = \left(\frac{P_{\text{inflow}}}{P_{\text{exit}}} \right)^{\frac{1}{\gamma}} \quad (14)$$

which is constant, allowing the density ratio to be moved outside of the integral in equation 12. For the more general case where the inflow density varies, the density ratio can be determined by setting the total density at inflow to that at the exit (along a streamline) giving:

$$\frac{\rho_{\text{inflow}}}{\rho_{\text{exit}}} = \left[\frac{1 + \left(\frac{\gamma-1}{2} \right) M_{\text{exit}}^2}{1 + \left(\frac{\gamma-1}{2} \right) M_{\text{inflow}}^2} \right]^{\frac{1}{\gamma-1}} \quad (15)$$

For an inflow radius of 1.0 and a centerline exit Mach number of 5.0 the theory gives an exit radius of 3.4199 and an exit static pressure of 2957.7 pascals.

Six nozzle contours were generated using the MOC with 15, 31, 65, 97, 135 and 201 inflow points. Smoothing of the contour was not needed for these cases. The error in the exit radius decreased monotonically from 0.0328 for the 15 point case to 0.00285 for the 201 point case, which corresponds to less than 1 percent error for the 15 point case and less than 0.1 percent error for the 201 point case. In all cases the exit static pressure exactly matched the theoretical value. A sample of the contour generated by the MOC is shown in figure 9. (On this scale all six contours look identical.) Figure 10 shows the total pressure profiles at the nozzle exit for the theory and for the MOC cases with 15, 31 and 65 points. (The other MOC profiles were very close to the theoretical curve and were left off the figure for clarity.) The maximum error in the total pressure profiles ranges from about 7.7 percent for the 15 point case to less than 0.6 percent for the 201 point case. The Mach number profiles at the nozzle exit were computed from the static and total pressures and are shown in figure 11. The maximum error in Mach number varied from about 1.35 percent for the 15 point case to about 0.11 percent for the 201 point case.

The order of accuracy of the method was determined by plotting the Log_{10} of the error in the exit radius versus the Log_{10} of the number of inflow points (see figure 12). The slope of the line verifies that this method is first order accurate.

While the theory is useful for evaluating the MOC exit radius and exit properties, it does not provide any information on the quality of the MOC generated contour. Instead, computational fluid dynamics (CFD) calculations on three grids were used. The three grid dimensions were 201x65, 401x129 and 801x257, where the first number is the number of points in the streamwise direction and the second number is the number of radial points. The contour used to generate the grids was computed by the MOC code using 65 inflow points. All three solutions were computed with the VULCAN code¹⁰ and the L_2 norm of the error reduced 14 orders of magnitude. The calculations were done assuming inviscid, calorically perfect flow. Contours of the Log_{10} of the static pressure are depicted in figure 13, which shows that the flow is accelerated smoothly to a constant static pressure without wave reflections. The maximum error in the exit total pressure profile for all three CFD solutions is less than 0.3 percent while the static pressure, shown in figure 14, is low by about 20 pascals (0.67 percent). Although low, the CFD computed static pressure is very uniform having a variation of only 0.34 percent. For all three CFD cases, the Mach number is high by about 0.15 percent. The slightly high Mach numbers and low static pressures are consistent with an exit radius that is slightly higher than the theoretical value. These low values of error verify the MOC nozzle design procedure and code.

III. HYPULSE Nozzle Design

The procedure for the design of the nozzle for the HYPULSE facility is similar to that for the verification-case nozzle. In this case, the inflow conditions were derived from an experimental pitot pressure profile of the HYPULSE tube exit at a Mach-15 flight-enthalpy condition.¹¹ The Mach number and static density were computed from the pitot profile assuming a constant static pressure of 198,215 pascals and a Crocco-Busemann temperature-velocity relationship.¹² The inflow profiles of Mach number and static density are shown in figures 15 and 16 respectively. The inflow was assumed to be parallel. At these operating conditions, there is only a 1.2 inch diameter core at the tube exit. As in the verification case, the expansion surface of the nozzle was specified as a Gaussian curve, with the radius of curvature at the inflow and the slope of the surface at the inflection point set by the user. For parallel exit flow, the specification of the expansion surface is the only input the user has in the design.

Although the user input is limited to specifying the radius of curvature and the inflection point slope, several trade-offs must be considered in the nozzle design process. On one hand, increasing the slope at the inflection point leads to a higher centerline exit Mach number and a longer nozzle. On the other hand, a small radius of curvature results in faster expansion of the flow and a shorter nozzle. However, viscous effects must also be considered. A long nozzle has a thicker boundary layer and a smaller core-flow size, whereas the rapid expansion of a nozzle with a small radius of curvature (shorter nozzle) can perturb or even separate the boundary layer introducing non-uniformities into the core flow. In addition, an MOC design with parallel exit flow always has a zero slope at the nozzle exit. In a viscous flow, the streamlines are displaced by the boundary layer and the flow near the MOC nozzle exit begins to recompress. As a result MOC designs are usually corrected for the boundary layer or truncated, which must be taken into account during the design process.

One other consideration in the design process is the non-uniformity of the nozzle inflow. Since total properties are constant along a streamline (equations 6 and 7), any non-uniformities in these properties present at inflow, will also be present at outflow.

The goal of the nozzle design effort was to produce a nozzle contour which, for the given tube exit profiles, produced acceptable conditions for testing a generic Mach-15 scramjet engine flowpath. Inlet entrance conditions were derived from an analysis of the forebody flowfield of a generic airbreathing launch vehicle flying at Mach 15. There was some flexibility in setting the target nozzle exit conditions based on the inlet conditions because the angle of attack of the test article could be varied to further process the flow between the nozzle exit and the engine inlet. In order to map the possible solution space, three nozzles with parallel exit flow and constant exit static pressures were designed with centerline exit Mach numbers of approximately 9, 9.5 and 10. Upon review of the solutions, the Mach-9 nozzle was selected.

The characteristic net and nozzle contour are shown in figure 17. This design was generated with a radius of curvature at inflow of 6 inches and a slope of 4.4 degrees at the inflection point. A γ of 1.32 was used which was representative of the values computed in a quasi-1D calculation with a variable γ thermodynamics model. The Mach-9 MOC contour is 98.4 inches long and has an area ratio of 9.6:1. Several contours were generated for this centerline exit Mach number using 15, 31, 65, and 101 inflow points. The exit Mach number profiles for each case are shown in figure 18 along with that from the theory (equations 12, 13 and 15). It is clear from this figure that the series of MOC designs has not converged to give the theoretical exit properties. Attempts to run cases with significantly larger numbers of inflow points were unsuccessful due to crossed characteristics.

To determine the quality of the contour generated using 101 inflow points, the nozzle flowfield was computed using CFD. Since the MOC contour had small protrusions of about 0.003 inch (and smaller), the contour was smoothed before generating the CFD grid. Figure 19 shows the slope of the surface before and after smoothing. Three inviscid, constant γ (1.32) CFD calculations were done with grid dimensions of 201x65, 401x129 and 801x257. A weak uncanceled pressure wave can be seen in figure 20 which shows contours of the Log_{10} of the static pressure. The exit static pressure profiles for all three CFD cases, and the theory are shown in figure 21. The static pressures of the CFD solutions are about 2 percent higher than the theoretical value for most of the exit profile but are about 6 percent higher near the centerline. The exit Mach number profiles are shown in figures 22 for the CFD solutions, the MOC solution (with 101 points) and the theory. It is interesting to note that the exit Mach number profiles from the CFD solutions match the theoretical profile better than the MOC profile.

The flowfield in the nozzle was also computed using viscous variable- γ CFD for both an adiabatic wall boundary condition and an isothermal boundary condition with the wall temperature set to 300 K. Both solutions were converged at least 10 orders of magnitude using a 301x201 grid. The Mach number profiles at the exit for the two cases are shown in figure 23. The difference in the profiles is due to the thicker boundary layer of the adiabatic wall case. The centerline exit Mach number for the adiabatic wall case is 8.7 while it is 8.78 for the isothermal wall case. Both cases have a core flow (defined by a 1 percent variation in Mach number) of about 3.6 inches in diameter, which is less than the theoretical value of 3.844. The static pressure profiles, shown in figure 24, have a pressure variation of about 3 percent, which is less than the exit pressure variation in the inviscid solution. This result may be due to the boundary layer displacement thickness smoothing the contour or viscous damping of weak uncanceled pressure waves.

As mentioned previously, MOC contours have a slope of zero degrees at the nozzle exit (for parallel exit flow). For viscous flow, the boundary layer displaces the streamlines and the flow near the exit begins to recompress. As a result the inviscid MOC contour is usually corrected by adding the displacement thickness at each axial location to the contour radial coordinate. An alternative is to simply truncate the nozzle at a point before the flow begins to recompresses and where the flow is still relatively uniform. For the current work the nozzle was truncated 82 inches from the inflow without any attempt to correct the centerline exit Mach number (the properties at this location were within the acceptable range). At the 82 inch location, the radius is 9.22 inches and the area ratio is 9.45. Profiles for the Mach number and static pressure at this location are shown in figures 25 and 26. At this axial location the centerline Mach numbers are slightly higher than at the exit; 8.72 for the adiabatic flow and 8.81 for the isothermal flow. Similarly, the pressures dropped about 0.3 percent while the variation in the pressure profiles stayed about the same (3 percent).

IV. Summary and Concluding Remarks

A new computer program has been written to design high-speed nozzles with non-uniform inflow profiles using the rotational method of characteristics. The program has been verified for a test case with a linear Mach number variation. The program has been applied to the design of a new nozzle for the HYPULSE shock-tube facility operating at a Mach-15 flight-enthalpy test condition. Although the MOC exit solution did not fully converge to the theoretical inviscid exit properties, the exit profiles were acceptable. The effects of the boundary layer were to reduce the centerline exit Mach number, increase the exit static pressure and

reduce the variation in the exit pressure profile to about 3 percent. The goal of increasing the test core size was achieved; increasing the core flow diameter from about 1.2 inches at inflow to about 3.6 inches at the exit (a factor of 9 increase in area).

References

- ¹Korte, J. J., "Inviscid Design of Hypersonic Wind Tunnel Nozzles for a Real Gas," AIAA paper 2000-0677, January, 2000.
- ²Sivells, J. C., "Aerodynamic Design of Axisymmetric Hypersonic Wind-Tunnel Nozzles," Journal of Spacecraft, Vol. 7, No. 11, pp. 1292-1299, November 1970.
- ³Korte, J. J., Private Communication, May, 2004.
- ⁴Gaffney, R. L., Jr., and Korte, J. J., "Analysis and Design of Rectangular-Cross-Section Nozzles for Scramjet Engine Testing," AIAA paper 2004-1137, January, 2004.
- ⁵Guy, R. W., Rogers, R. C., Puster, R. L., Rock, K. E. and Diskin, G. L., "The NASA Langley Scramjet Test Complex," AIAA paper 96-3243, July, 1996.
- ⁶Zucrow, M. J., Hoffman, J. D., *Gas Dynamics*, Volume II, John Wiley and Sons, New York, 1977.
- ⁷Anderson, J. D., Jr., *Modern Compressible Flow With Historical Perspective*, McGraw-Hill Book Co., New York, 1982.
- ⁸Genkin, L., Baer, M. and Falcovitz, J., "Gasdynamic Approach to Small Plumes Computation," Journal of Spacecraft and Rockets, Vol. 31, No. 4, pp. 691-700, July-August 1994.
- ⁹Press, W. H., Teukolsky, S. A., Vetterling, W. T., and Flannery, B. P., *Numerical Recipes in FORTRAN, The Art of Scientific Computing, Second Edition*, Press Syndicate of the University of Cambridge, New York, 1992.
- ¹⁰White, J. A. and Morrison, J. H., "A Pseudo-Temporal Multi-Grid Relaxation Scheme for Solving the Parabolized Navier-Stokes Equations," AIAA paper 99-3360, June, 1999.
- ¹¹Rogers, R. C., Private communication, October, 2003.
- ¹²Chue, R., "CFD Calculation of HYPULSE SET Nozzle for Mach 15-H16 Condition," GASL R&AD Technical Note No. 158, July, 2003.

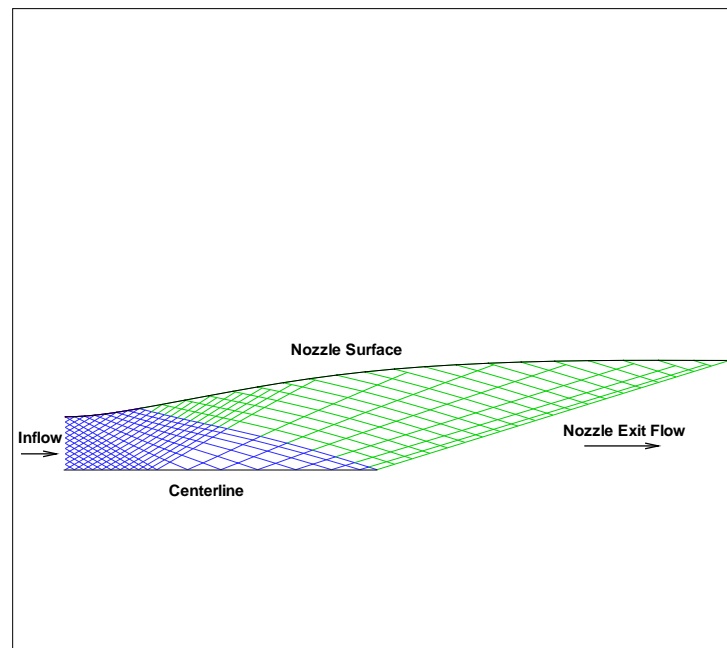


Figure 1. Example of a characteristic net in a nozzle flow field.

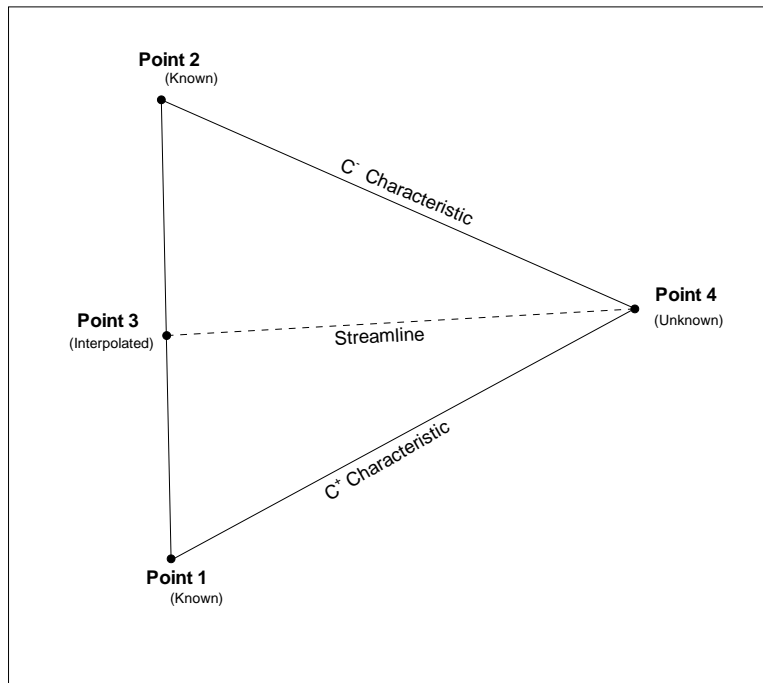


Figure 2. Schematic of the interior kernel-point geometry.

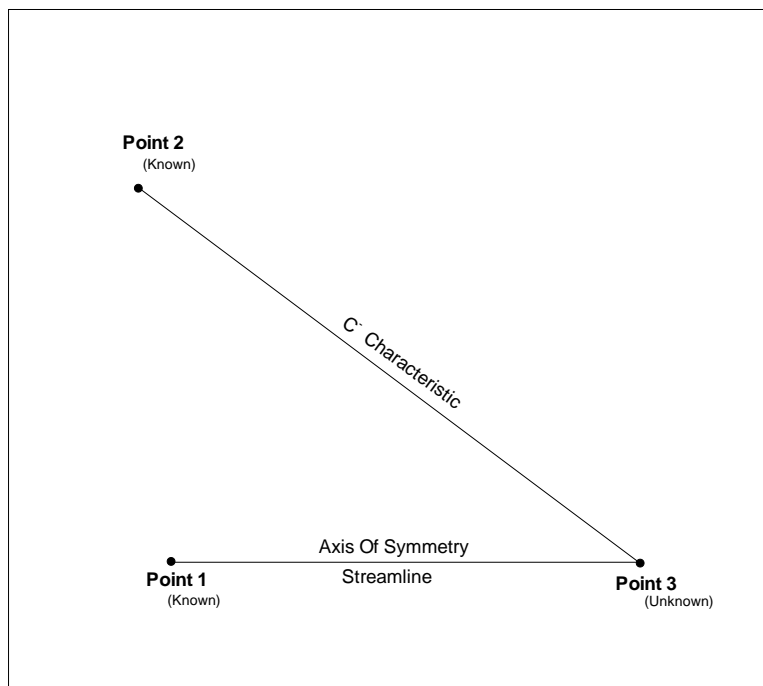


Figure 3. Schematic of a centerline point geometry.

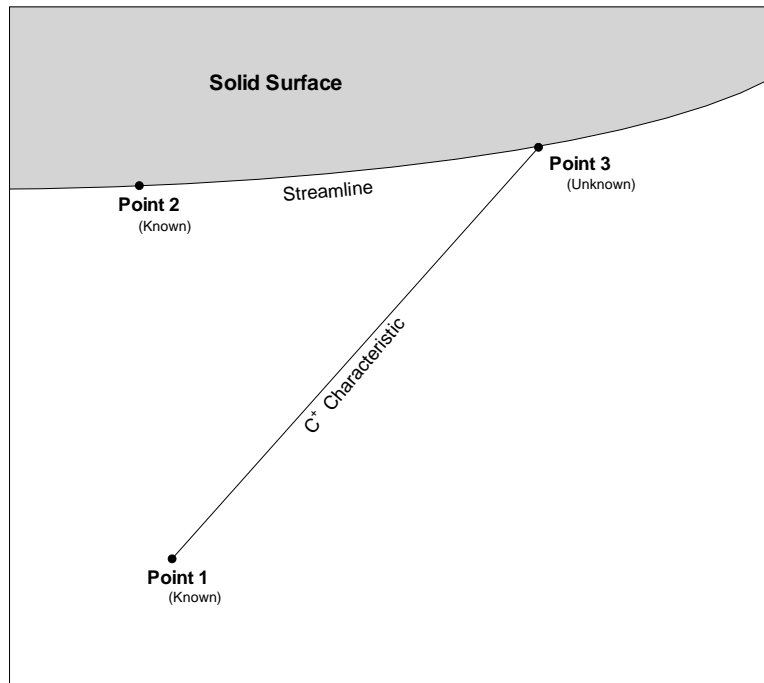


Figure 4. Schematic of a solid surface point geometry.

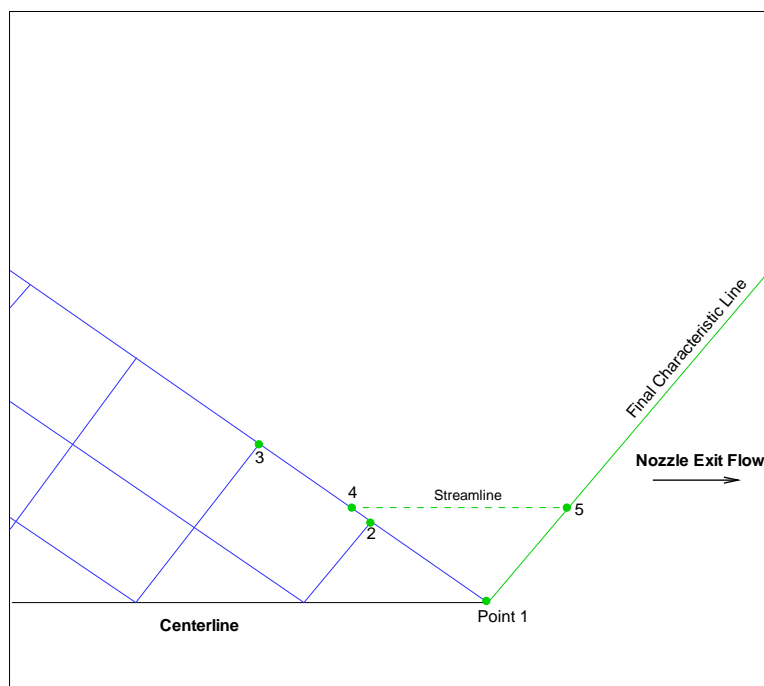


Figure 5. Schematic of a final characteristic point geometry.

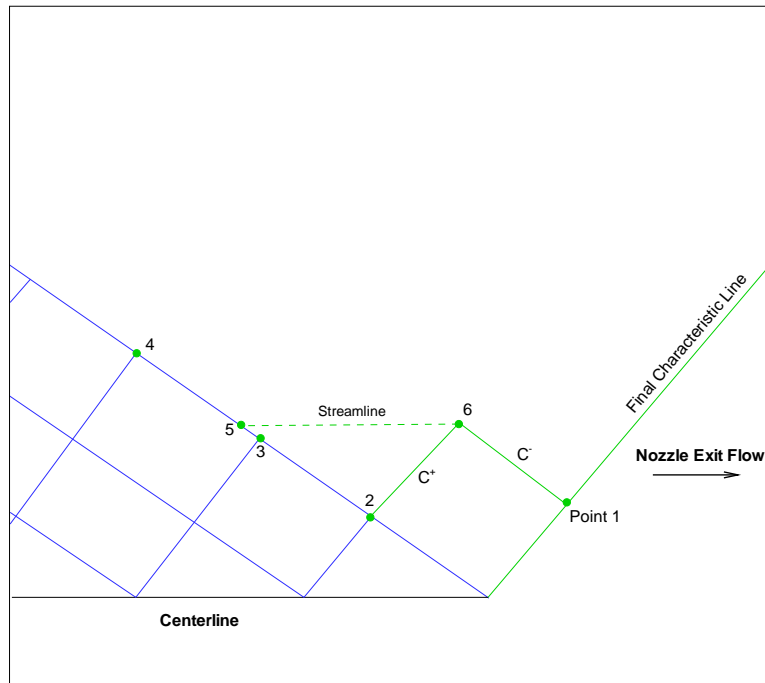


Figure 6. Schematic of an interior point (turning region) geometry.

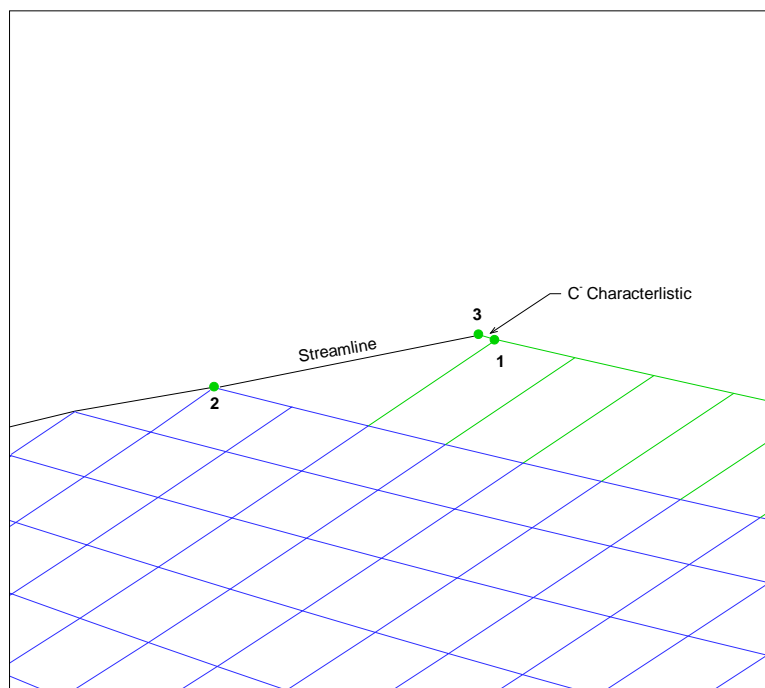


Figure 7. Schematic of a surface point (turning region) geometry.

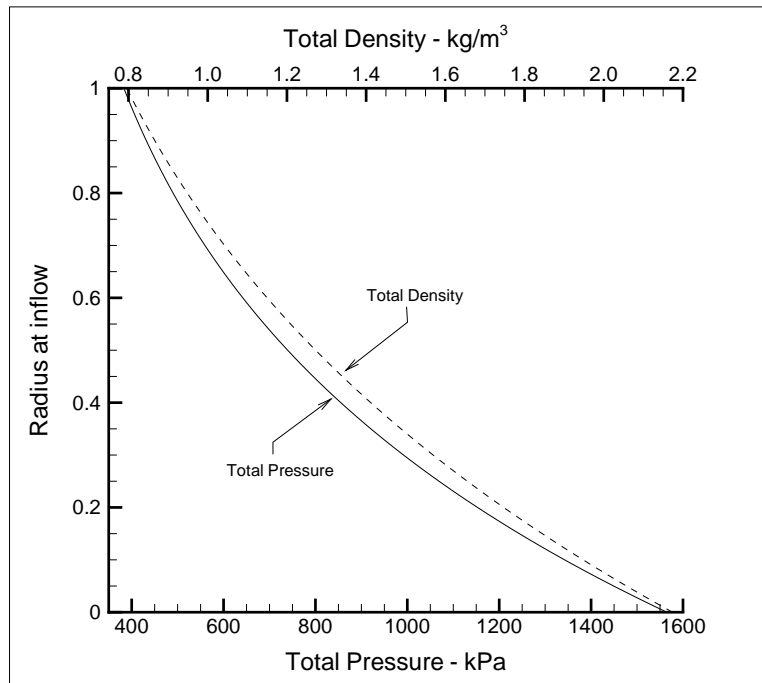


Figure 8. Verification-case total pressure and total density inflow profiles.

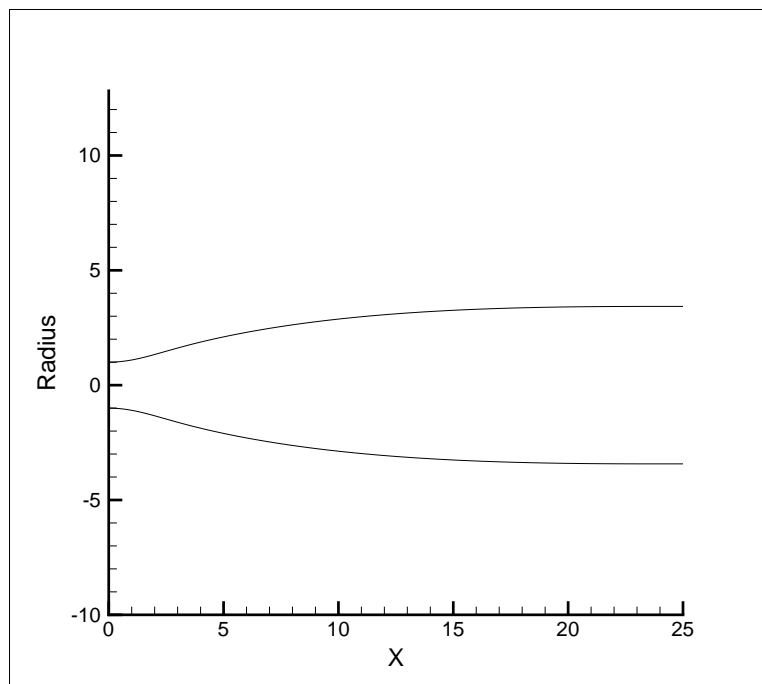


Figure 9. Verification-case MOC contour.

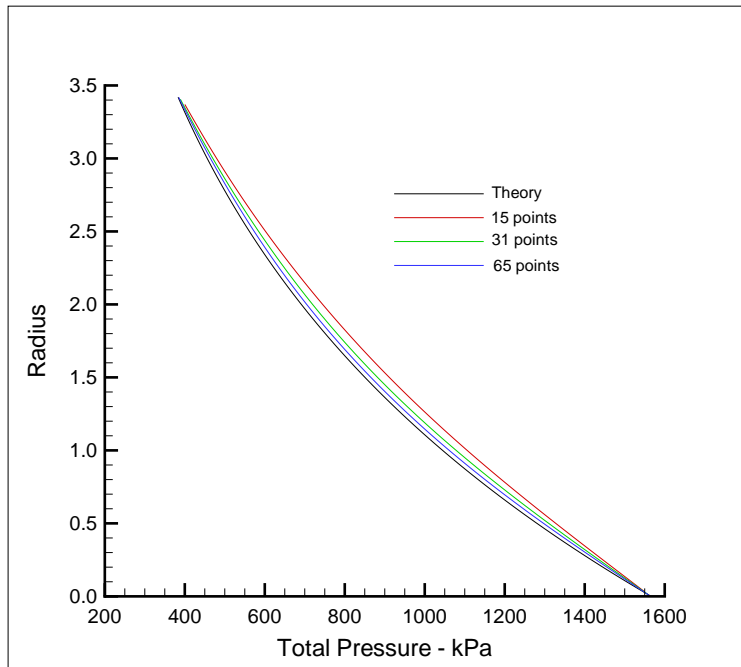


Figure 10. Theoretical and MOC total pressure profiles at the nozzle exit. The three MOC solutions are for different numbers of inflow points.

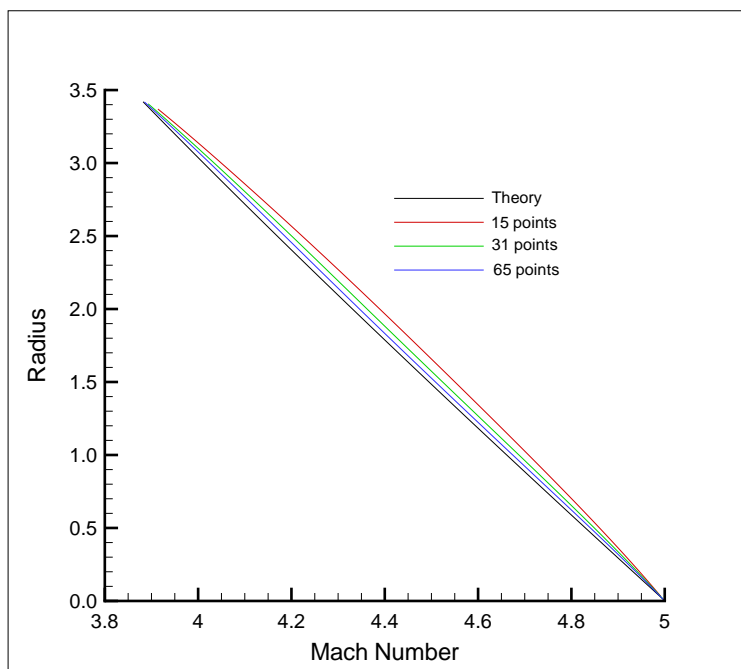


Figure 11. Theoretical and MOC Mach number profiles at the nozzle exit. The three MOC solutions are for different numbers of inflow points.

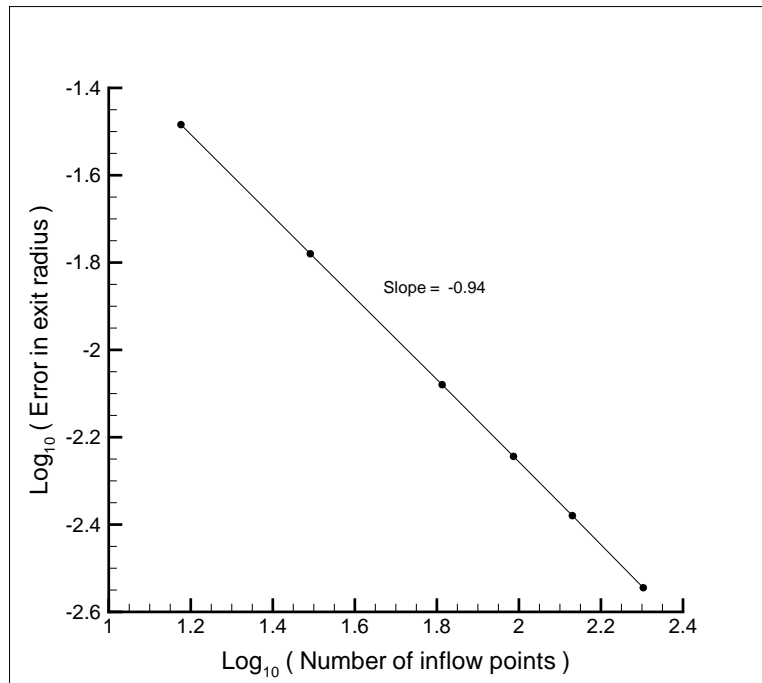


Figure 12. Error in exit radius vs. number of points, convergence property.

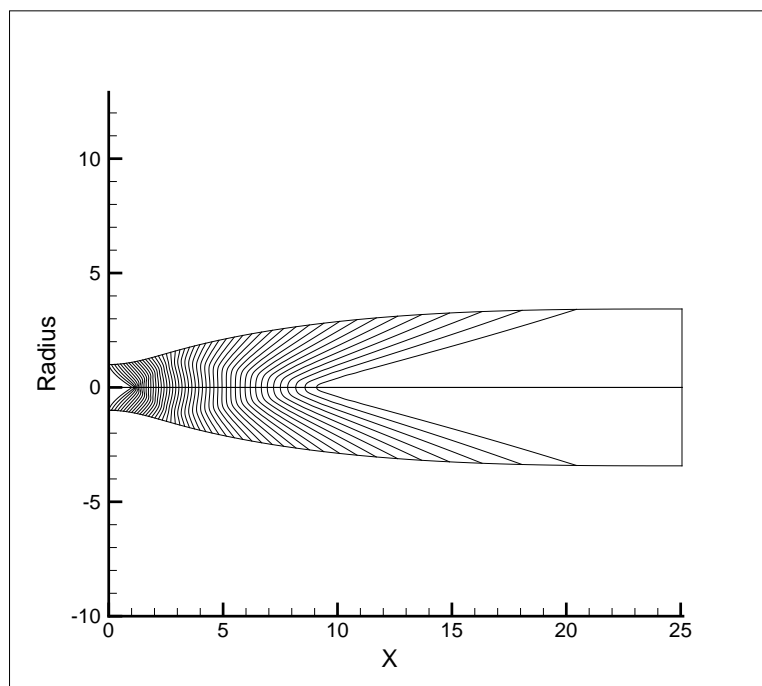


Figure 13. CFD contours of $\log_{10}(\text{static pressure})$ in the nozzle.

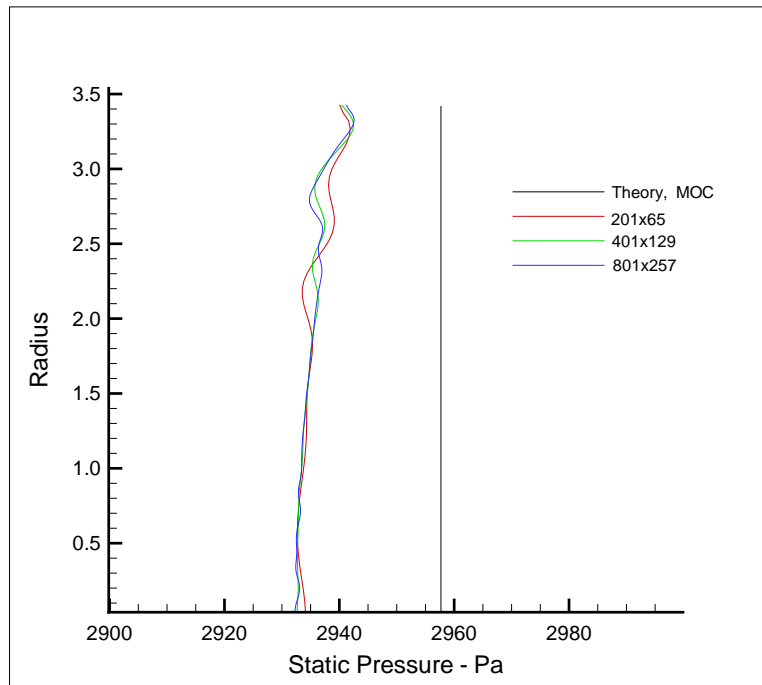


Figure 14. Theoretical, MOC and CFD static pressure profiles at the nozzle exit.

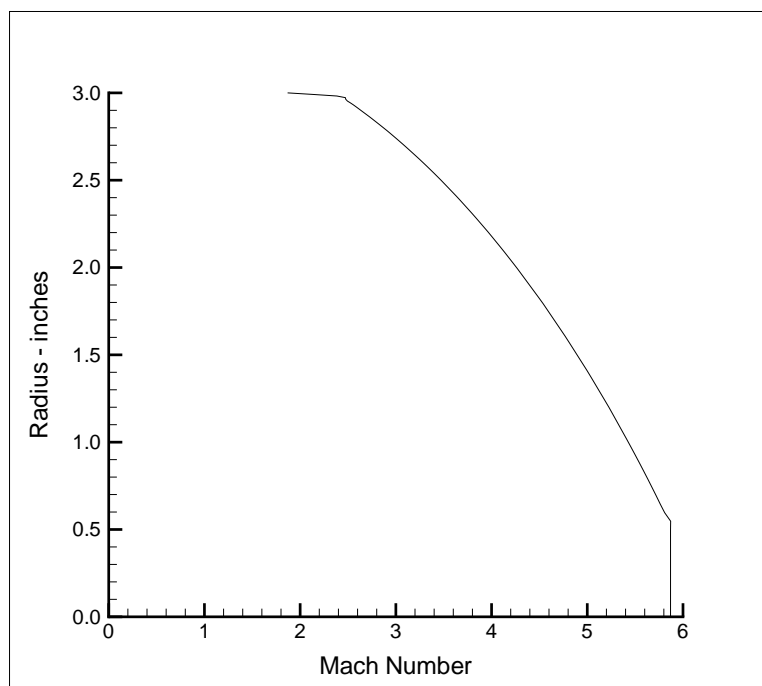


Figure 15. Nozzle inflow profile of Mach number.

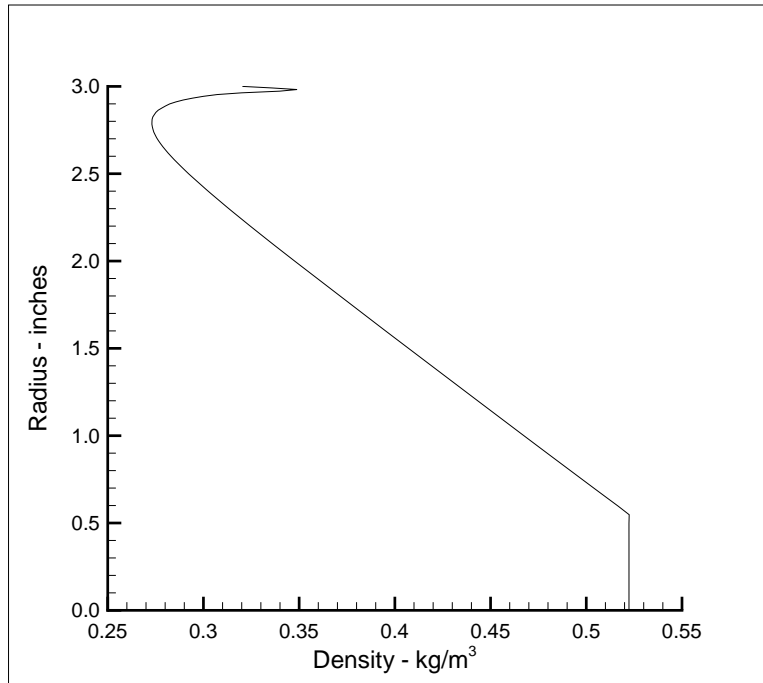


Figure 16. Nozzle inflow profile of density.

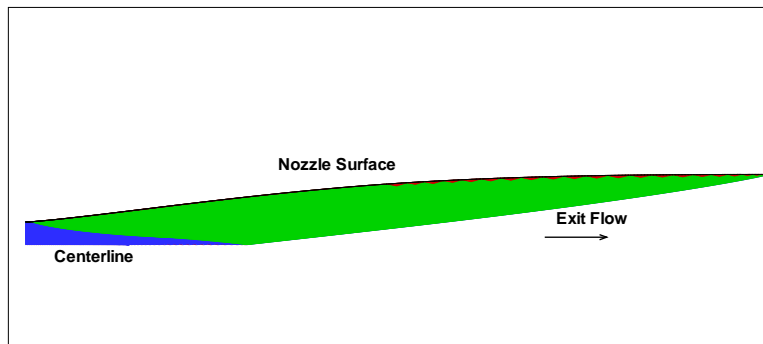


Figure 17. Final MOC design.

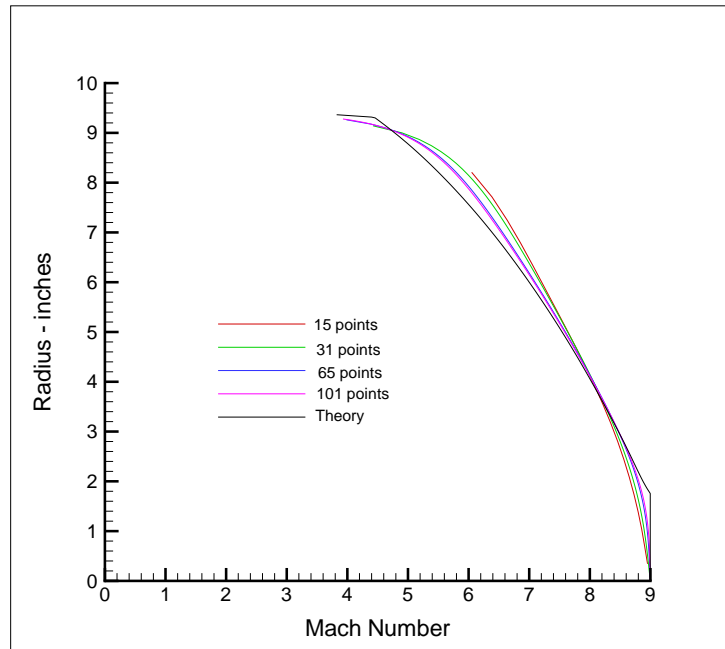


Figure 18. Theoretical and MOC Mach number profiles at the nozzle exit. The four MOC solutions are for different numbers of inflow points.

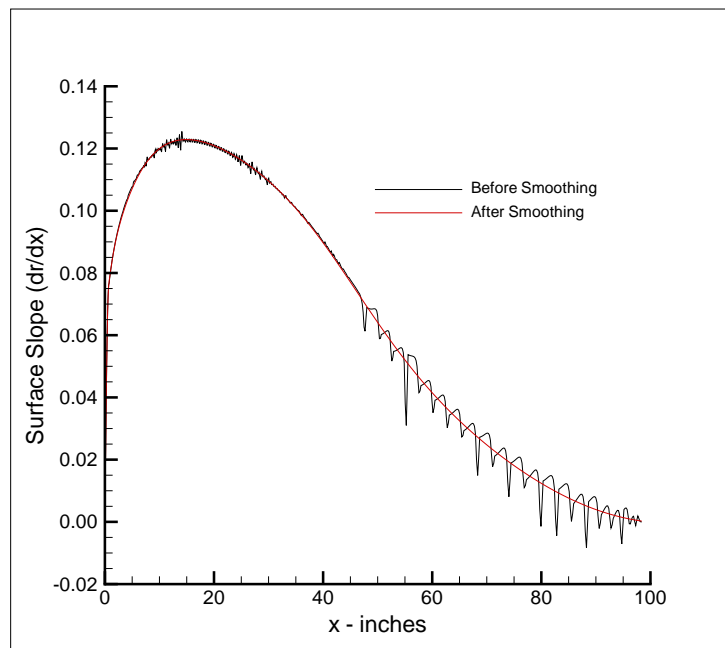


Figure 19. Surface slope of the MOC contour before and after smoothing.

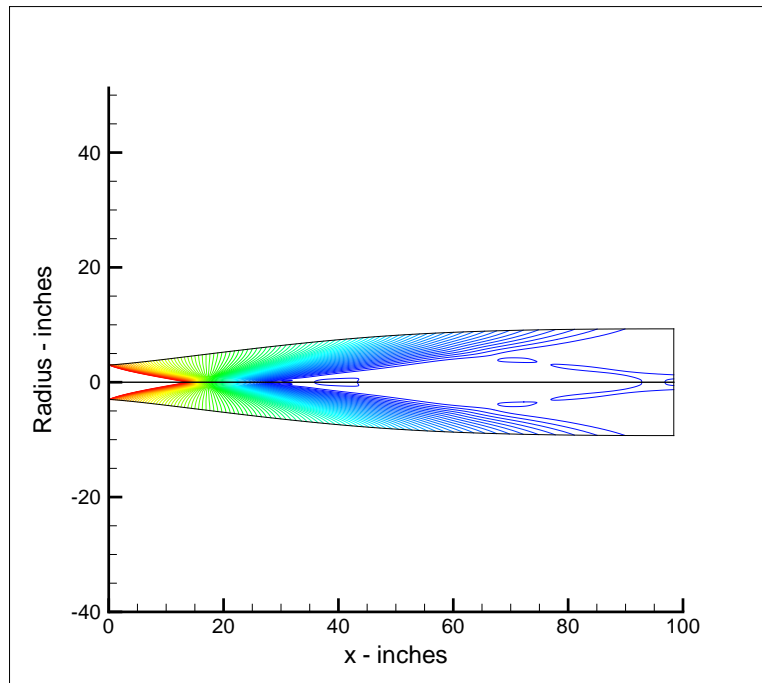


Figure 20. CFD contours of the Log_{10} (static pressure) in the final design nozzle

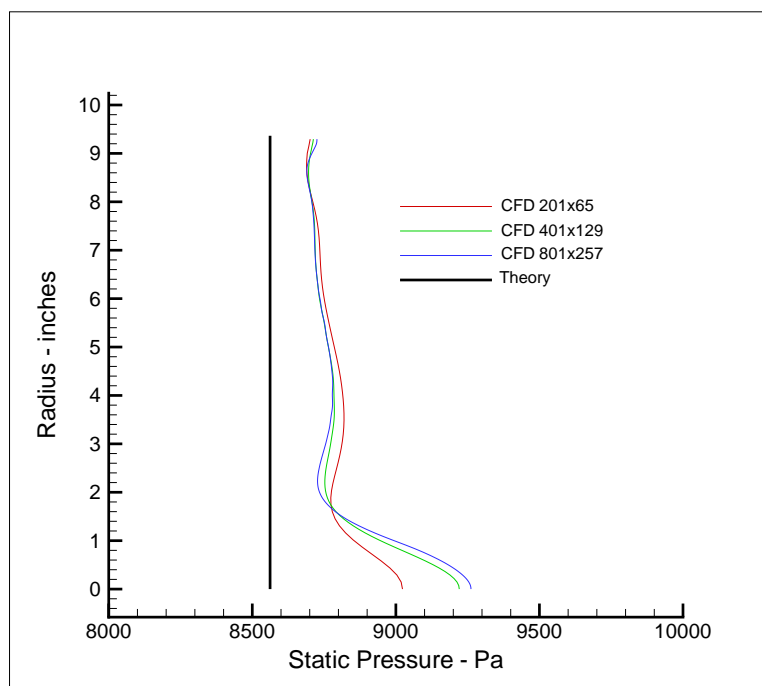


Figure 21. CFD, MOC and theoretical pressure profiles at the nozzle exit.

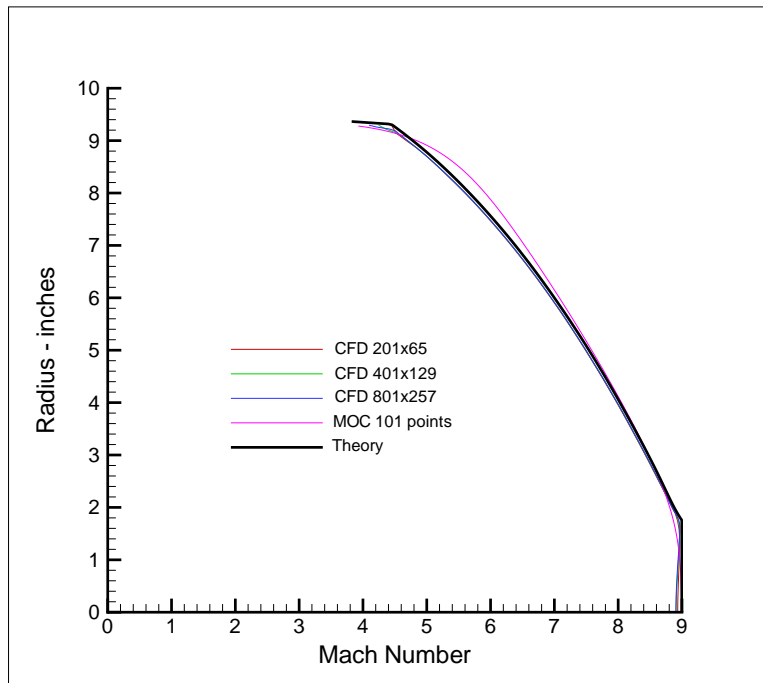


Figure 22. CFD, MOC and theoretical Mach number profiles at the nozzle exit.

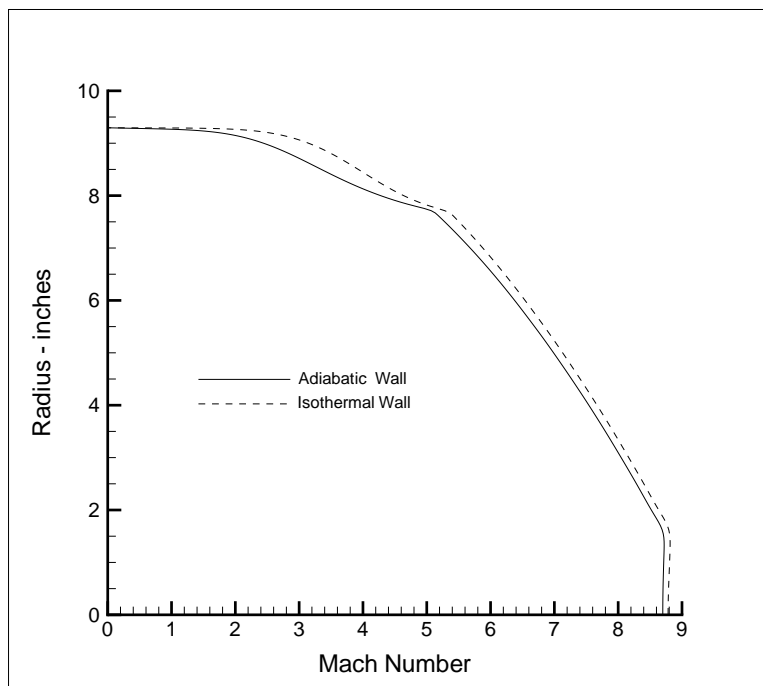


Figure 23. CFD Mach number profiles at the nozzle exit for adiabatic and isothermal wall cases.

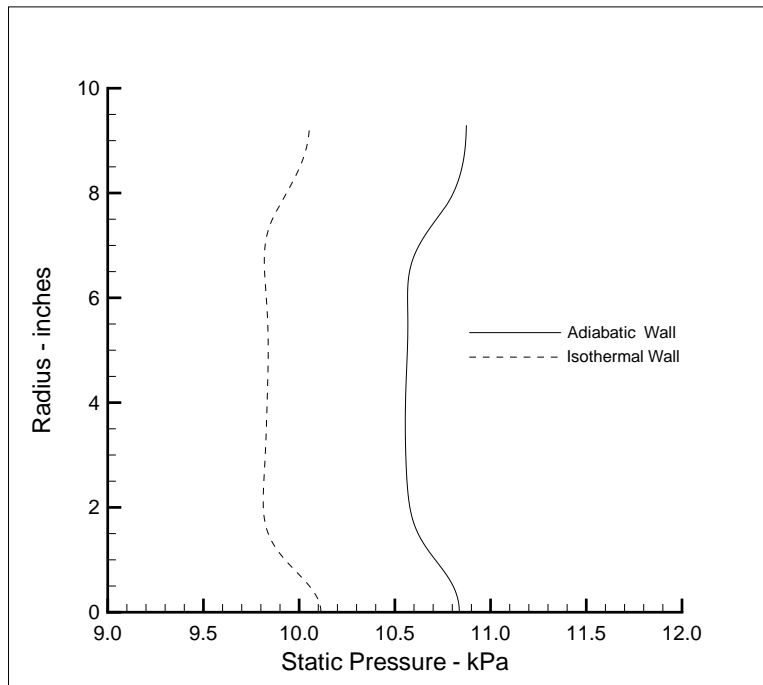


Figure 24. CFD pressure profiles at the nozzle exit for adiabatic and isothermal wall cases.

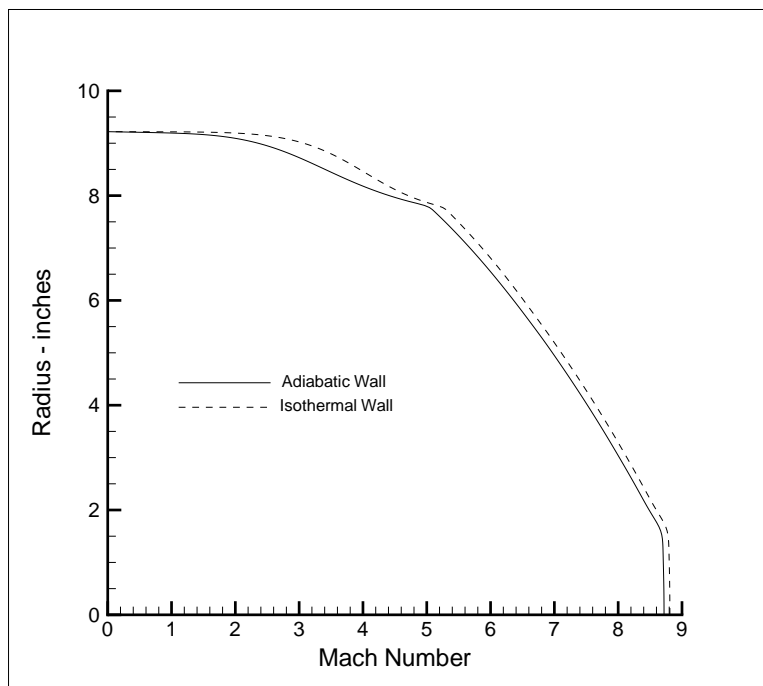


Figure 25. CFD Mach number profiles at 82 inches for adiabatic and isothermal wall cases.

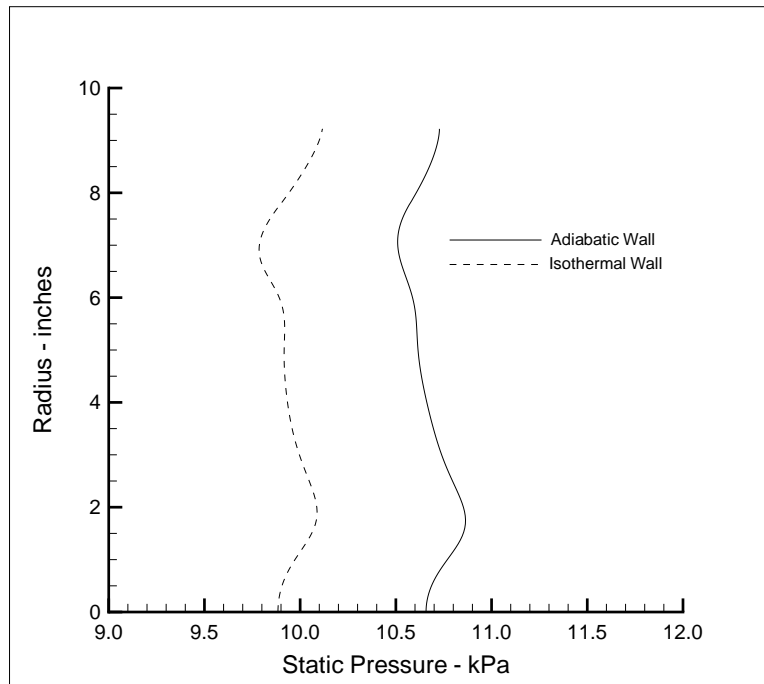


Figure 26. CFD pressure profiles at 82 inches for adiabatic and isothermal wall cases.